Chinese Chemical Letters 35 (2024) 108648

Contents lists available at ScienceDirect

Chinese Chemical Letters

journal homepage: www.elsevier.com/locate/cclet

A coating strategy on titanium implants with enhanced photodynamic therapy and CO-based gas therapy for bacterial killing and inflammation regulation[☆]

Liang Cheng[a], Bingshuai Zhou[b], Manlin Qi[a], Xiaolin Sun[a], Shujun Dong[a], Yue Sun[a,*], Biao Dong[b,*], Lin Wang[a,*], Yingwei Yang[a,c,*]

[a] *Department of Oral Implantology, Jilin Provincial Key Laboratory of Sciences and Technology for Stomatology Nanoengineering School and Hospital of Stomatology, Jilin University, Changchun 130021, China*
[b] *State Key Laboratory on Integrated Optoelectronics, College of Electronic Science and Engineering, Jilin University, Changchun 130021, China*
[c] *College of Chemistry, Jilin University, Changchun 130012, China*

ARTICLE INFO

Article history:
Received 28 April 2023
Revised 31 May 2023
Accepted 5 June 2023
Available online 7 June 2023

Keywords:
Photodynamic therapy
Biomaterials
Dental implant
Reactive oxygen species
Carbon monoxide
Hybrid nanoplatform

ABSTRACT

Antimicrobial photodynamic therapy (aPDT) has been considered a noninvasive and effective modality against the bacterial infection of peri–implantitis, especially the aPDT triggered by near-infrared (NIR) light due to the large penetration depth in tissue. However, the complexity of hypoxia microenvironments and the distance of aPDT sterilization still pose challenges before realizing the aPDT clinical application. Due to the long lifespan and transmission distance of therapeutic gas molecules, we design a multi-functional gas generator that combines aPDT as well as O_2 and CO gas release function, which can solve the problem of hypoxia (O_2) in PDT and the problem of inflammation regulation (CO) in the distal part of peri–implant inflammation under near-infrared (NIR) irradiation. In the composite nanoplatform that spin-coated on the surface of titanium implants, up-conversion nanoparticles (UCNPs) were involved in converting the NIR to visible, which further excites the partially oxidized stannic sulfide (SnS_2), realizing the therapeutic gas release. Indocyanine green (ICG) was further integrated to enhance the aPDT performance (Ti-U@SnS_2/I). Therefore, reactive oxygen species (ROS), CO, and O_2 can be controllably administered *via* a composite nano-platform mediated by a single NIR light (808 nm). This implant surface modification strategy could achieve great self-enhancement antibacterial effectiveness and regulate the lingering questions, such as relieving the anoxic microenvironment and reaching deep infection sites, providing a viable antibiotic-free technique to combat peri–implantitis.

Implantation is defined as teeth substitute insertion for partially and completely edentulous patients, with an estimated more than two million implants per year stunningly. However, a 5%−11% probability of failure after 10–15 years of implantation is still a non-negligible matter [1]. Dental implant biological failures are primarily due to the accumulation of bacterial plaque and pathogenic infectious, known as peri–implantitis, causing biological complications and affecting the local immune microenvironment [2]. Further notice is that the deep infection in peri–implantitis causes it extremely difficult to cure.

Surface antibacterial modification of implants based on nanomaterials and nanotechnology is an important solution to this problem. Some research groups, including us, have explored the modification methods of antibacterial nanomaterials on the surface of Ti implants, such as CeO_2, black phosphorus, and zinc oxide [3–6], and achieved effective antibacterial near the implants by using photothermal, photodynamic or chemical dynamic treatments (CDT), playing a vital role in promoting the treatment of peri–implantitis [7–9]. However, PDT induced by conventional photosensitizers (PSs) is stimulated by red light (<660 nm) and is difficult to reach deep infection sites. In particular, the antibacterial effect of the antimicrobial photodynamic therapy (aPDT) triggered by near-infrared (NIR) light has been proven to be very effective since NIR light owns a powerful tissue penetration depth (almost 5–10 mm) to reach the surface of the implant in deep tissue [10]. During this process, the PSs are modified on the implant's surface.

[☆] This paper is dedicated to the memory of Prof. Jiang Wei.

[*] Corresponding authors.

E-mail addresses: sunyueyue@jlu.edu.cn (Y. Sun), dongb@jlu.edu.cn (B. Dong), wanglin1982@jlu.edu.cn (L. Wang), ywyang@jlu.edu.cn (Y. Yang).

https://doi.org/10.1016/j.cclet.2023.108648

After the NIR light reaches the photosensitizer on the surface, the PSs can be excited and further convert the nearby oxygen into singlet oxygen, thus achieving efficient sterilization [11].

Before realizing the aPDT clinical application, two practical medical problems must be considered. Firstly, the critical problem is the hypoxic environment in the deep site of the periodontal pocket, which limits the oxygen supply in aPDT process, seriously affecting the antibacterial performance. Furthermore, the hypoxic microenvironment is also a recognized propellant for inflammation and could exacerbate the degree of peri–implantitis [12,13]. Secondly, aPDT sterilization aims to achieve effective inflammation regulation within a relatively short distance of the implant, especially within 0.2 cm of the implant [14]. Mostly, progressive bone loss of peri–implant marginal out of 2 mm range, and an increase in probing depth from the baseline much exceeded 5 mm [15]. However, for the distance from the surface of the implant to the outside, there are practical difficulties in the large-scale regulation of inflammation based on the surface antibacterial modification of implants because the transmission distance and existence life of free radicals are very short compared to the scope of influence of peri–implant inflammation.

Since gas molecules have a longer life span and transmission distance than free radicals, introducing a regulatory gas molecular generator on the implant will be an effective method to achieve relatively long-distance inflammation regulation near the implant. Especially, producing gas molecules with the aid of environmental factors at the focal site could be an effective solution to comfort hypoxia and regulate inflammatory situations. In our previous exploration, we established the oxygen-self-supply manganese dioxide (MnO_2)-based nanoplatform and introduced the NIR light to trigger the aPDT process to figure out the hypoxia phenomenon for antibacterial treatment [16], suggesting that the establishment of gas bomb treatment at the site of infection may be effective. It is known that partially oxidized stannic sulfide (SnS_2) nanosheets are a promising candidate material with several advantages, such as low toxicity, cheap cost, and stable chemical properties [17]. Two-dimensional partial SnS_2 could generate high efficiency of CO and O_2 under the stimulation of visible light [18]. The latest studies have indicated that CO could regulate anti-inflammatory, and the mechanism of CO-mediated effects may be associated with anti-inflammation [19]. Thus, as a gas generator, SnS_2 would be expected to deal with both troublesome issues under light irradiation.

However, how to use a single light source to complete the function of stimulating aPDT and SnS_2 is still triggered in the therapeutic process. Up-conversion nanoparticles (UCNPs), which could convert a longer wavelength radiation (NIR) to a shorter wavelength radiation (visible light) according to an anti-Stokes process, have great potential use as a bio-photoconverter in the treatment of deep infection [20]. The special properties of UCNPs provide us with more in-depth thinking for the establishment of our target nanoplatform. On account of this research, we provide the thought to introduce the up-conversion capability into the PDT system, convert NIR into visible light, and provide a promising method for further optimizing the excitation light source of SnS_2 NSs.

In this work, based on the specificity of peri–implant inflammation, the NIR-triggered up-conversion fluorescence technology is combined with CO and O_2 generation performance of SnS_2. As a proof-of-concept, we prepared an optimized coating to multi-functional modify the Ti surface. The hybrid nanoplatform integrating UCNPs, SnS_2, and indocyanine green (ICG, photoexcited nanomaterial) (Ti-U@SnS_2/I) was developed with CO and O_2 generation properties for anti-microbial and anti-inflammation. As demonstrated in Scheme 1, in this nano-system, ROS, CO, and O_2 were controllably administered *via* a composite nanomaterial platform mediated by a single NIR source (808 nm) which can be converted to visible light by UCNPs to further excite the partially oxidized SnS_2 nanosheets. It is worth mentioning that this nano-coating could not only achieve great self-enhancement antibacterial effectiveness, but also realize effective inflammation regulation in a wide range near the implant. This CO-based aPDT treatment system would provide a viable antibiotic-free technique to combat peri–implantitis, and it could be a promising new mentality for clinical medicine development.

The core-shell structure morphology of the synthesized UCNPS was confirmed by TEM and DLS (Figs. 1A and B), which showed that the structural morphology of the NPs mainly remained unaltered. The average diameter of the inner core NPs was between 31.15 ± 0.48 and 35.65 ± 0.97 nm, and that on the shell layer was between 46.75 ± 0.53 and 51.15 ± 0.29 nm. XRD patterns indicated that the homogeneous core and shell layers of UCNPs were successfully synthesized (Fig. 1C). The results conformed to the hexagonal $NaYF_4$ standard card (JCPDS No. 28–1192) [21]. The flake nanostructure of partially oxidized SnS_2 nanosheets was seen in the TEM picture (Fig. 1D1) and SEM (Fig. 1D2). Fig. 1E displayed the TEM and SEM images of U@SnS_2 nanosheets. The distribution of UCNPs could be observed on the surfaces of the nanosheets, which were labeled by blue circles and yellow arrows in Fig. 1E (E1 and E2).

As shown by the 2D image (Fig. 1F1) and 3D image (Fig. 1F2) of the AFM, the nanomaterials on the surface of the modified Ti sheets are of uniform thickness, large specific surface, rough texture, and constant roughness. The AFM analysis provided that the quick and straightforward approach to surface modification allowed for effective coating thickness control. The SEM image of Fig. 1G also proved that there was a constant and well-distributed coating on the surface of Ti disks. To sum up, the progression of modifying the U@SnS_2/I NSs has been showed in Fig. 1H. Firstly, the core and shell of the UCNPs in the nanoplatform has been exhibited in Figs. 1A and B), and the package was completed by hydrothermal method as showed in Fig. 1H. After the preparation of SnS_2 (Fig. 1D), U@SnS_2 nanosheets were synthesized by another hydrothermal method (Fig. 1H), Fig. 1E also proved the successful synthesis under the condition. Subsequently, U@SnS_2 nanosheets were further modified by SH-PEG to load the ICG onto the nanosheets, as the exhibition in Fig. 1H. The final composite U@SnS_2/I was also successfully proved in Fig. 1G.

The XRD patterns of Fig. 2A showed that the characteristic peaks of SnS_2 appeared at 28.30° and 50.00°, and the characteristic peaks of UCNPs appeared at 7.1°, 29.8°, 30.6°, 43.3°, and 53.5° All the peaks appeared in the XRD pattern of U@SnS_2, which validated the presence of UCNPs and SnS_2. In our design, U@SnS_2 NSs were modified with the polymer SH-PEG to produce multifunctional nanomaterials in the next stage. Then the ICG photosensitizer was electrostatically adsorbed on the surface of the modified U@SnS_2/PEG nanomaterials to prepare U@SnS_2/I nanocomposites. According to the FTIR spectra of Fig. 2B, the co-existence between U@SnS_2 and ICG was confirmed. The presence of SnS_2 was proved by the band of 550 cm^{-1} assigned to the Sn-S groups, and the presence of ICG was verified through peaks of C=C groups at 1413.9 cm^{-1} [22]. The absorption peaks of SnS_2 and ICG in the UV–vis absorption spectra of U@SnS_2/I also indicated the presence of SnS_2 and ICG in U@SnS_2/I (Fig. 2C). In addition to further confirming the nanocomposite formation, the zeta potentials were measured in Fig. 2D. The zeta potential value switched from +13.3 mV to −17.7 mV after loading with ICG.

For U@SnS_2/I NSs, it was essential to detect the ROS-generating efficiency and the photocatalytic efficiency of U@SnS_2 NSs by up-conversion triggering. UCNPs could absorb two or more low-frequency photons and then emit one high-frequency photon, which could convert NIR light to visible light with an anti-Stokes process, showing great potential in treating deep infection [23]. It

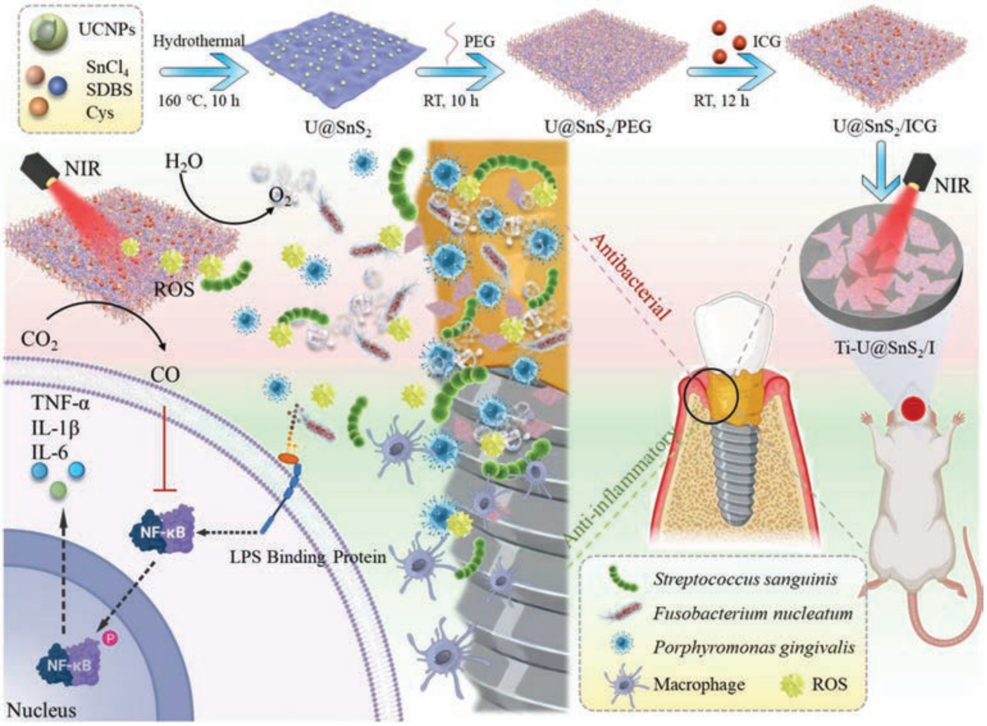

Scheme 1. Schematic diagram of the Ti-U@SnS$_2$/I preparation, the steps of its synthesis, and its design for peri–implantitis antimicrobial action and inflammation-modulating function. The modified Ti surface was excited by NIR (808 nm) to produce a large amount of ROS to produce antibacterial, while the concomitant production of O_2 further enhanced the effectiveness of the antibacterial photodynamic, the release of CO improved the antibacterial killing efficiency, achieving the inhibition of the inflammatory immune response of peri–implantitis by regulating the secretion of inflammatory cytokines. U@SnS$_2$ represented the nanosheet with UCNPs and SnS$_2$. U@SnS$_2$/PEG represented the nanosheet of U@SnS$_2$ multi-functionalized by PEG. U@SnS$_2$/I represents the nanosheet with UCNPs, SnS$_2$, and ICG. Ti-U@SnS$_2$/I represents U@SnS$_2$/I coated on a pure Ti surface.

is known that the energy transfer process of up-conversion can be influenced by the distance between the receptor and the donor, therefore, the emission spectra of UCNPs and U@SnS$_2$ NSs were tested. The results in Fig. 2E showed that the emission intensity of U@SnS$_2$ NSs was significantly decreased under 808 nm excitation. Due to their close combination of UCNPs and U@SnS$_2$ NSs, this result suggested a non-radiative energy transfer process between them. The fluorescence lifetime was tested to ulteriorly pinpoint the energy transfer mechanism (Fig. 2F). The fluorescence lifetime of U@SnS$_2$ NSs was shorter than that of pure UCNPs under the same excitation conditions, which is consistent with the emission spectra. The above results demonstrated that U@SnS$_2$/I system could provide enough energy to activate the SnS$_2$ and ICG to produce CO and O_2 under the irradiation of NIR.

In this design, the U@SnS$_2$/I could be excited by NIR irradiation and generate ROS effectively along with the production of CO and O_2. In addition, the O_2 would further promote the ROS production [24]. The aPDT and gas production properties of U@SnS$_2$/I were investigated by the ROS, CO, and O_2 generation tests. The ROS production of U@SnS$_2$/I was monitored as displayed in Fig. 2G, the absorption value of the DPBF probe at 420 nm gradually decreased after exposure to NIR light for 25 min, which indicated that ROS could be created efficiently during light exposure. Since the CO probe has green fluoresce under PdCl$_2$-catalyzed, as displayed in Fig. 2H, the intensity at 522 nm was monitored and found steadily increase, which proved the continuous generation of CO. Fig. 2I showed that the light intensity was gradually diminishing at 628 nm, indicating that there was a continuous generation of oxygen during the 25 min. These test results supported the hypothesis that the generation of self-supplied oxygen from U@SnS$_2$/I could address the local hypoxic microenvironment and boost ROS production.

The ROS production rates of SnS$_2$/I and U@SnS$_2$/I by NIR light were mostly identical at the beginning stage, and decreased gradually in the later stages due to the lack of raw oxygen material in the SnS$_2$/I group, whereas there was still more ROS production in the U@SnS$_2$/I group due to the self-supply of O_2 Fig. S1 (Supporting information). In addition, results based on CCK-8 assay and histological analysis of rats' major organs indicated the overall safety of the Ti-U@SnS$_2$/I and their potential in further (Figs. S2 and S3 in Supporting information).

Owing to the limitation of O_2 diffusion in biofilm, the O_2 tension in deep infection sites seriously decreased [25]. However, O_2 played a significant role in the aPDT process since photosensitizers needed to transfer energy with oxygen molecules to make ROS. Such an anoxic microenvironment at peri–implantitis sites would severely hamper the function of aPDT against bacteria. In the present study, Ti-U@SnS$_2$/I could convert H_2O into O_2 *via* the SnS$_2$ catalysis, which plays positive action on ROS generation, improving the antibacterial effect (Fig. 3A). The biofilm formed by the deposition of pathogenic bacteria on the implant surface was the initiating factor for peri–implantitis [26,27]. First, *Porphyromonas gingivalis* (*P. gingivalis*) was selected as the primary pathogen of peri–implantitis to assess the antibacterial capacity of Ti-U@SnS$_2$/I. The 3D live/dead staining results are shown in Fig. 3B. A large amount of live bacteria by green staining was present in the control group and Ti-U@SnS$_2$ group. The dead bacteria by red staining showed an increasing tendency in the Ti-SnS$_2$/I group, because bacteria were killed by ROS generation of Ti-SnS$_2$/I. ROS, the main weapon in aPDT to kill bacteria, could directly react with proteins, nucleic acids, extracellular polymers, and other biomolecules in super-oxidative reactions, resulting in the cell wall and organelle damage [28]. Interestingly, dead bacteria of the Ti-U@SnS$_2$/I group were more than the Ti-SnS$_2$/I group. That indicated the O_2 gener-

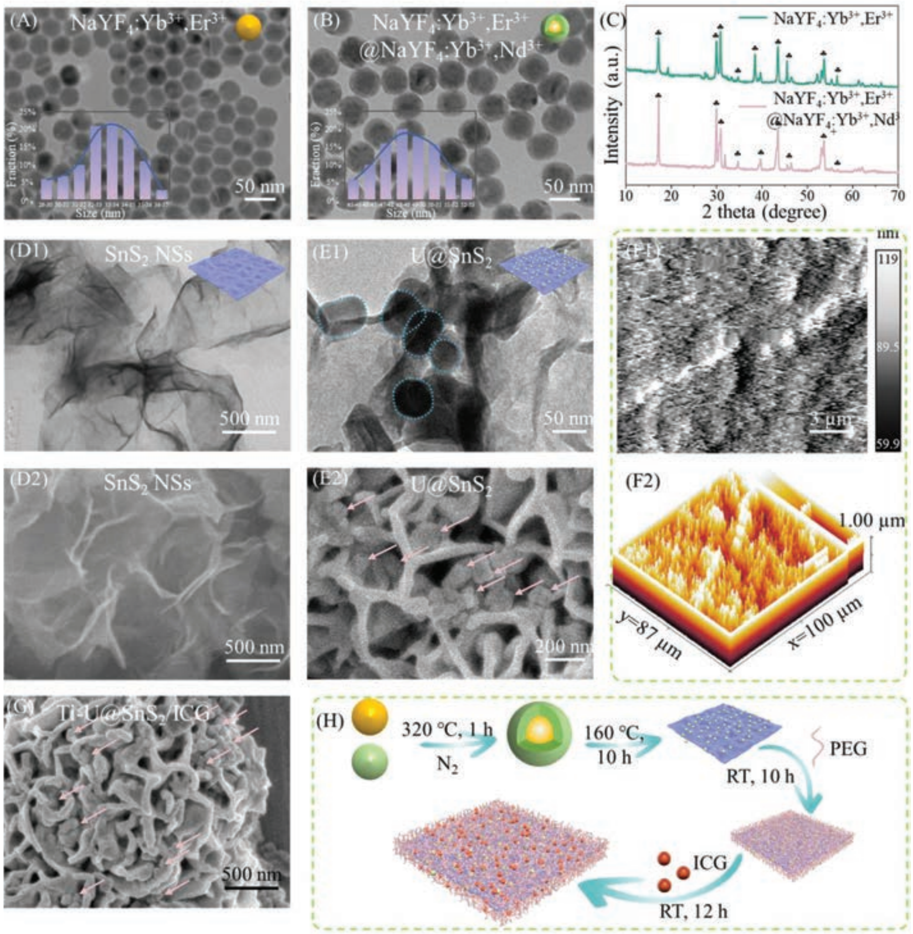

Fig. 1. Synthesis and characterization of U@SnS_2/I. TEM pictures of (A) $NaYF_4$:Yb^{3+},Er^{3+} and (B) $NaYF_4$:Yb^{3+},Er^{3+}@$NaYF_4$:Yb^{3+},Nd^{3+}. The illustration of Figs. 1A and B: the histograms of UCNPs average size distribution. (C) XRD of core and core @ shell. (D1) TEM and (D2) SEM images of SnS_2. (E1) TEM and (E2) SEM images of U@SnS_2. (F1) 2D and (F2) 3D AFM images of Ti sheet surface films. (G) SEM images of Ti-U@SnS_2/I. (H) Scheme of preparation of U@SnS_2/I. The blue circles in (E1) and the yellow arrows in (E2) and (G) indicate the UCNPs.

ation of Ti-U@SnS_2/I enhanced the aPDT treatment. The dead/live bacterial ratio was highest in the Ti-U@SnS_2/I groups (Fig. 3C). As displayed in Fig. 3D, the metabolic activity significantly declined in the Ti-SnS_2/I group and Ti-U@SnS_2/I group contrasted with the control group, especially in Ti-U@SnS_2/I group. Figs. 3E and F depicted the CFU of *P. gingivalis* with different dilution concentrations. Compared with the control group, CFU values for the Ti-SnS_2/I group had an approximate reduction of 3 orders of magnitude. While the Ti-U@SnS_2/I group got an approximate 1-log CFU reduction compared with Ti-SnS_2/I group. This confirmed again that Ti-U@SnS_2/I produced O_2, promoting the aPDT antibacterial efficiency. Similar trends were present in the *Fusobacterium nucleatum* (*F. nucleatum*) results (Figs. S4 and S5 in Supporting information). Ti-U@SnS_2/I also demonstrated the most excellent antibacterial capacity against *F. nucleatum*. In addition, *Streptococcus sanguinis* (*S. sanguinis*), as the early adherent bacteria, were performed to further evaluate the antibacterial capacity. The live/dead stain results revealed that the Ti-U@SnS_2/I group had the highest percentage of dead bacteria, accounting for 73.87%, while the dead bacteria in Ti-SnS_2/I accounted for 65.2% (Figs. S6A and B in Supporting information). The results of the 4-hour bacterial metabolic activity assay of *S. sanguinis* were similar to the live/dead stain results (Fig. S6C in Supporting information). To summarize, Ti-U@SnS_2/I could reverse the hypoxic environment in deep periodontal pockets, provide enough oxygen to the aPDT, and encourage ROS formation to attain excellent antimicrobial efficacy.

Microbial invasion of the surrounding pocket-like binding epithelium triggers the host immune defense response in peri–implantitis. With the gradual dysregulation of the microenvironment, the innate immune mode is over-activated and leads to the rapid destruction of the surrounding tissue of the implant [29]. Also, the aPDT could sterilize by producing ROS, but the inflammation reaction is still a complex problem. As illustrated in Fig. 4A, CO generation could induce the switch of macrophage polarization from the M1-phenotype to the M2-phenotype, which would restrain the local over-immune response, reduce inflammatory damage, and accelerate the regenerative potential [30].

In order to investigate the immunomodulatory function of Ti-U@SnS_2/I on the inflammatory response, macrophages were stimulated with *P. gingivalis*-LPS to simulate the inflammatory microenvironment, and the release of pro-inflammatory-related factors was investigated by RT-qPCR. As shown in Fig. 4B, macrophages in the control group generated a large amount of pro-inflammatory molecules by stimulating LPS, including IL-6, TNF-α, and IL-1β. The stronger expression of pro-inflammatory-related factors in the Ti-SnS_2/I group were found due to oxidative stress reaction by local high-concentration free radicals. ROS, as a pro-inflammatory mediator, easily penetrates macrophages membranes, leading to cell

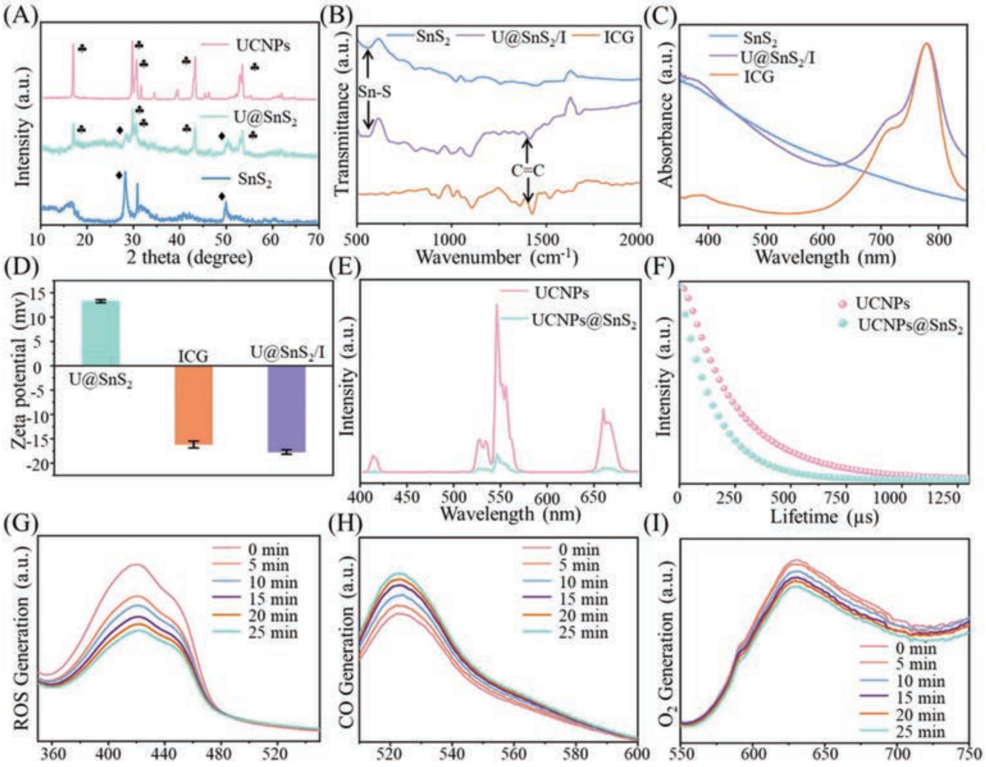

Fig. 2. Characterization of U@SnS_2/I and release of ROS, CO, and O_2 generation rates from U@SnS_2/I composite nanomaterials under 808 nm excitation. (A) XRD analysis of UCNPs, U@SnS_2, and SnS_2. (B) FTIR and (C) UV–vis-NIR absorption spectra of SnS_2, U@SnS_2/I, ICG. (D) Zeta potential of U@SnS_2, ICG, U@SnS_2/I. (E) Emission spectra of UCNPs and U@SnS_2. (F) The fluorescence lifetime of UCNPs and U@SnS_2. Dynamic values of (G) ROS, (H) CO, and (I) O_2 generation of U@SnS_2/I under 808 nm excitation condition.

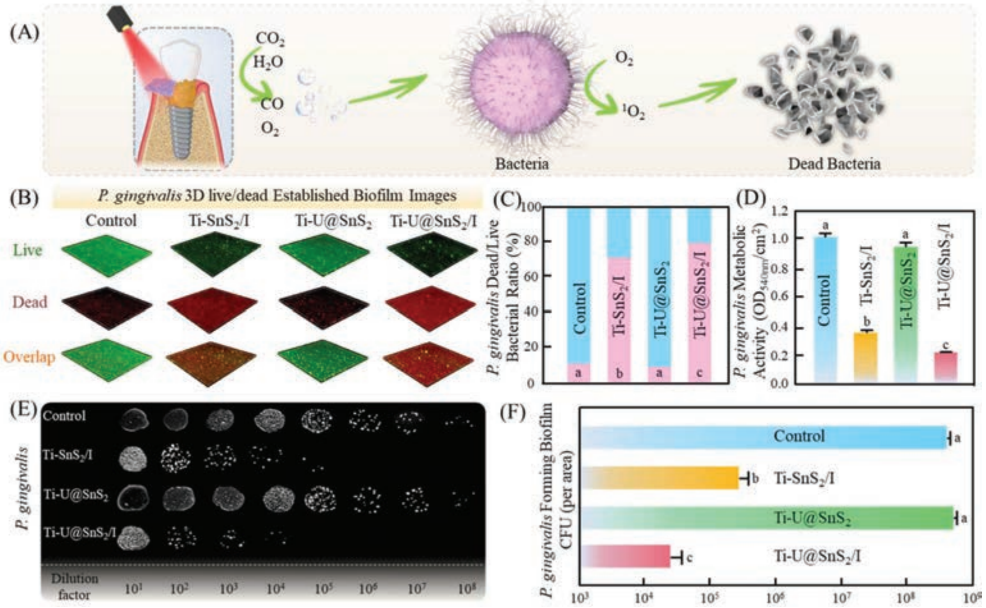

Fig. 3. (A) Scheme of the antimicrobial effect of Ti-U@SnS_2/I on peri–implantitis. (B) Representative 3D live/dead images and (C) live/dead bacteria ratio of *P. gingivalis* on the Ti sheet surface. (D) MTT assay for the *P. gingivalis*. (E) The colony formation images and (F) statistical counts of *P. gingivalis*. ($n = 3$, $P < 0.05$).

structure disruption, mitochondrial dysfunction, oxidative damage and even cell death, therefore, more pro-inflammatory substances were secreted by macrophages [31]. Both the Ti-U@SnS_2 and Ti-U@SnS_2/I groups had presented the reduction of pro-inflammatory factor secretion and inhibition of M1 polarization of macrophages, indicating that CO played a highly effective anti-inflammatory role in both groups. As depicted in Fig. 4C, the results demonstrated that the M2 phenotype macrophages related mRNA expression of anti-inflammatory factors in Ti-U@SnS_2 and Ti-U@SnS_2/I groups were upregulated compared with the control groups because of the increase of CO content in the local microenvironment. UCNPs transfer the NIR to the visible light, activating the SnS_2 to

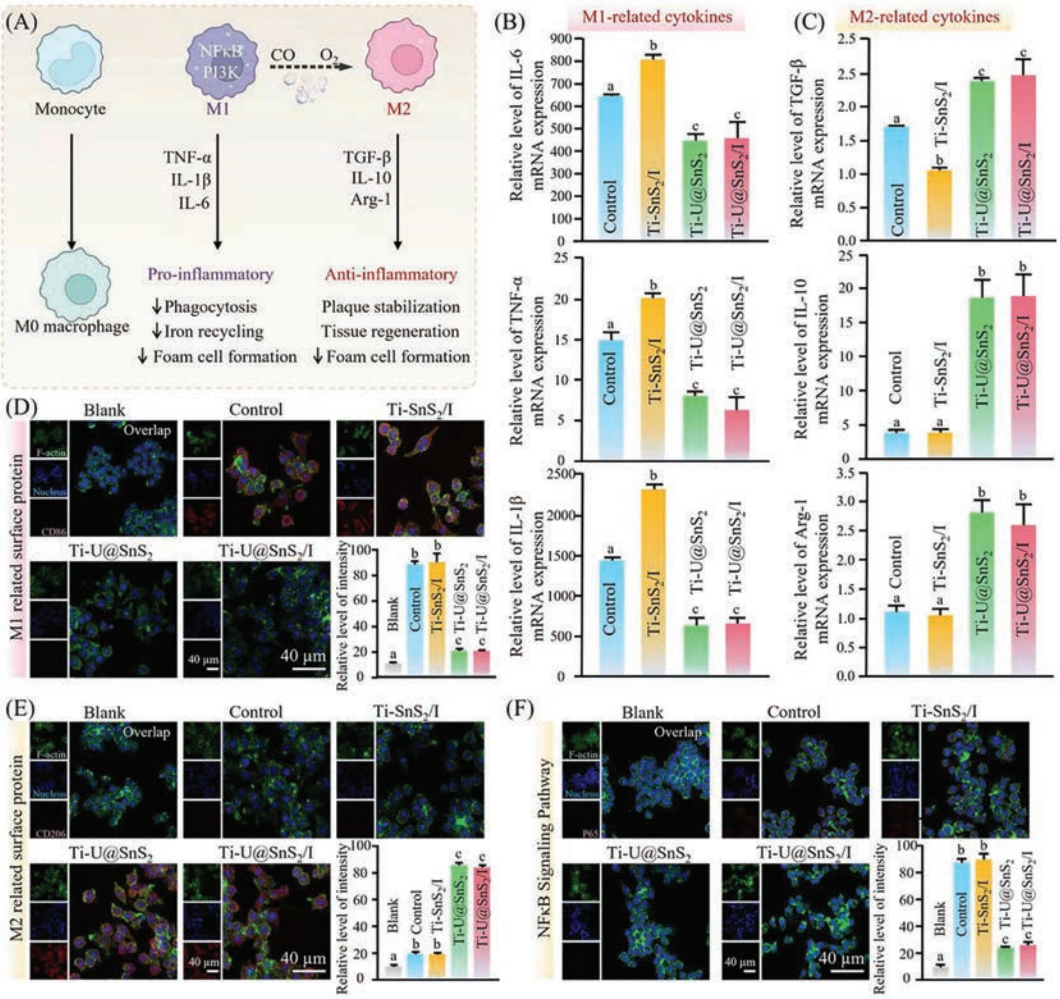

Fig. 4. Anti-inflammatory property of Ti-U@SnS$_2$/I. (A) Schematic image of the macrophage switching from the M1-phenotype to the M2-phenotype. (B, C) RT-qPCR analysis the related mRNA level of pro-inflammatory cytokines including (M1 markers: IL-6, IL-1β, TNF-α) and anti-inflammatory cytokines including (M2 markers: TGF-β, IL-10, Arg-1) after *P. gingivalis*-LPS (1 μg/mL) stimulating for 3 h (Ti blank without *P. gingivalis*-LPS was calibrated as "1", $n = 3$, mean ± sd). (D, E) Immuno-fluorescent images and the statistical quantification of positive cells of M1-phenotype and the M2-phenotype related surface protein expression. (F) Immunofluorescent images and the quantification of NF-κB/p65 translocation ($n = 3$, $P < 0.05$).

release CO. Previous studies have shown that the CO could inhibit local inflammation [32]. Notably, the immune system maintains homeostasis *via* positive and negative feedback regulators. The pro-inflammatory related factors and anti-inflammatory related factors present a crucial role in organism inflammation. The pro-inflammatory factors IL-6, TNF-α, and IL-1β amplified inflammatory signaling through positive feedback effects, while the M2-phenotype related factors, including TGF-β, IL-10, Arg-1, and other anti-inflammatory factors, acted as negative feedback effects to inhibit inflammatory signaling [12]. Ti-U@SnS$_2$/I could induce the reduction of pro-inflammatory related factors and the increase of anti-inflammatory related factors, keeping the immune balance and facilitating the repair and healing of inflamed tissues.

Fluorescence labeling was used for M1 macrophage-specific protein CD86, and M2 macrophage-specific protein CD206 to further confirm the phenotypic impact of CO signaling molecules in the local microenvironment on regulatory macrophages [33,34]. Fig. 4D illustrated that after LPS stimulation, both the control and Ti-SnS$_2$/I group displayed stronger fluorescence intensity than the other groups in the CD86 immunofluorescence test. In contrast to Fig. 4D, the immunofluorescent intensity of CD206 was much stronger in the Ti-U@SnS$_2$ and Ti-U@SnS$_2$/I group as shown in Fig. 4E. It confirmed that the Ti-U@SnS$_2$/I under irradiation (808 nm) could regulate the polarization phenotype of macrophages, inhibiting the cascade response of macrophages and promoting the regenerative effect of tissue.

The NF-κB signaling pathway is a significant immunoregulation pathway. After LPS inducing, the nuclear transcription factor NF-κB/p65 entered the nucleus and bound to the NF-κB site on the enhancer, subsequently transcription and translation of corresponding inflammatory genes were initiated, finally a large number of regulatory reactants such as IL-6, TNF-α, and IL-1β were produced, damaging the tissue [35,36]. The NF-κB/p65 protein fluorescence staining was further explored. As depicted in Fig. 4F, the p65 protein fluorescence intensity was strongly expressed in the control groups due to the excitation of NF-κB signaling pathway by LPS. On the contrary, both the groups of Ti-U@SnS$_2$ and Ti-U@SnS$_2$/I exhibited lower p65 protein fluorescence intensity due to the CO release after NIR irradiation. Thus, Ti-U@SnS$_2$/I could restrain the process of NF-κB/p65 entering the nucleus and then regulate the immune response, achieving the anti-inflammatory effect.

We screened the mRNA expression data compatible with the involvement of CO in anti-inflammatory in this experiment from the GEO database [37] to further detect the changes at the mRNA level caused by LPS and CO. All the up-regulated and down-regulated genes obtained by these two comparative experiments were shown

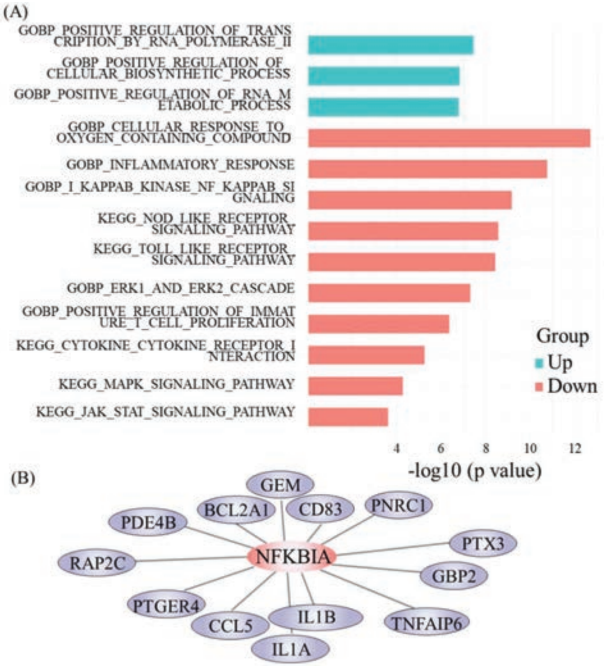

Fig. 5. Anti-inflammatory mechanism of Ti-U@SnS_2/I. (A) The up-regulation and down-regulation genomic alterations of signaling pathways caused by CO. (B) Differential co-expression genes which are highly co-expressed with NFKBIA in the LPS+CO group but not in the LPS group. Different letters represent statistical differences among each group ($n = 3$, $P < 0.05$).

as the volcano plots ($P < 0.05$, |log2foldchange| > 1) (Figs. S7 and S8 in Supporting information), and the heatmap was illustrated in Fig. S9 (Supporting information). Compared with the blank group, the expression of pro-inflammatory genes, such as CXCL2, IL-1β, TNF, IL-1A, were significantly up-regulated in the LPS group, indicating that LPS exposure induced inflammation as expected. On the other hand, compared with the LPS group, the expressions of IL-1A, IL-1β, CXCL3, and NFκB1A were significantly down-regulated in the LPS+CO group. That demonstrated most proinflammatory genes were strongly expressed in the LPS group; however, when the CO interference, proinflammatory genes were weakly expressed.

To explore the function of each differentially expressed gene set, we conducted pathway and biological function enrichment analysis and indicated that the CO-suppressed genes were significantly enriched in the NF-κB signaling pathway ($p < 0.05$), toll-like receptor signaling pathway ($p = 3.87 \times 10^{-9}$), MAPK signaling pathway ($p = 5.56 \times 10^{-5}$) and JAK-STAT signaling pathways ($p = 2.57 \times 10^{-4}$) (Fig. 5A). Moreover, we further detected NFκBIA informative differential co-expression genes, which simultaneously satisfied two conditions: (i) differentially expressed between the LPS+CO group and LPS group; and (ii) highly correlated with NFκBIA in the LPS+CO group but not in the LPS group. All the obtained differential co-expression genes of NFκBIA were shown in Fig. 5B. The NFκBIA gene encoded IκBα was down-regulated under CO exposure. IκBα is one of the inhibitory proteins of NF-κB pathway excitation, which limits the translocation of NF-κB nuclear transcription factors into the nucleus and down-regulates associated pro-inflammatory factors to attenuate the inflammatory response [38]. Many inflammation-related genes (IL-1A, IL-1β) encoded pro-inflammatory factors also decrease along with the NFκBIA gene. These results were consistent with our results that CO can regulate inflammatory-related factors according to the NF-κB signaling pathway.

In vitro tests have shown that the Ti-U@SnS_2/I had a strong antibacterial and anti-inflammatory effect, but we also need to prove the *in vivo* therapeutic impact with peri–implantitis. The entire procedure of the *in vivo* experiment is depicted in Fig. 6A, Ti sheets with various modified surfaces were implanted under the keratinized gingiva of rats. The mixture bacteria (*S. sanguinis*, *F. nucleatum*, *P. gingivalis*, 1:1:1, 10^8 CFU/mL, 0.02 mL) were injected around the Ti sheets. Then the subcutaneous Ti sheets were irradiated with NIR every day. As shown in Fig. 6B, the soft tissue around the Ti sheets healed slowly and parts of Ti sheets were still exposed for 7 days in the control group. The Ti-U@SnS_2 group with solo CO generation and Ti-SnS_2/I group with solo ROS generation displayed relatively favorable healing and the tissues were almost healed up at 7 days. Ti-U@SnS_2/I groups exhibited the most excellent and fastest tissue healing since aPDT treatment synergistic CO therapy exerted positive antibacterial effects and immunoregulation. As shown in Fig. 6C, a mass of bacterial colonies could be observed in the control group and Ti-U@SnS_2 group, while a small number of colonies could be found in the Ti-SnS_2/I group and the Ti-U@SnS_2/I group due to the ROS generation. The biofilm scavenging efficiency was most outstanding in the Ti-U@SnS_2/I group. This result was attributed to Ti-U@SnS_2/I enhanced aPDT *via* O_2 generation.

In Fig. 6D, the results of the H&E stain and IHC stains revealed pathological alterations and inflammatory responses in the gingival tissue around the Ti sheets. In H&E staining, the control group displayed tremendous amounts of inflammatory cells in the gingival tissues. Compared with the control group, the Ti-SnS_2/I group and the Ti-U@SnS_2 group had fewer inflammatory cells. Notably, the Ti-U@SnS_2/I represented the lowest number of inflammatory cells. Moreover, in IHC staining images, Ti-U@SnS_2/I group had the lowest expression of the pro-inflammatory-related factor IL-1β and the highest expression of the anti-inflammatory-related factor Arg-1. These results were because Ti-U@SnS_2/I could generate O_2 to enhance the antibacterial capacity of aPDT treatment, lessening the bacteria-induced inflammation. Meantime it could produce CO to further relieve the inflammation. Then, the distribution of collagen in the implant site was analyzed by Masson staining (Fig. 6E). The pathogenic bacteria could directly destroy the collagen and indirectly induce inflammation for collagen degradation [39]. The Masson staining results demonstrated that the destruction of the collagen was obvious in the control group. Mass collagen degradation was in the Ti-U@SnS_2 group due to the great numbers of bacteria survival. The collagen degradation significantly decreased in the Ti-SnS_2/I group. This may be attributed to the fact that the bacteria reduction was induced *via* aPDT treatment. Interestingly, the Ti-U@SnS_2/I group had the least collagen degradation. The reason may be that Ti-U@SnS_2/I possessed excellent antibacterial capacity and CO generation to regulate immune response, synergistically alleviating the antimicrobial-induced inflammatory damage.

We then conducted another implant infection model to verify the therapy efficiency of Ti-U@SnS_2/I as an aPDT synergic CO gas treatment. The Ti sheets with various modified surfaces were implanted under the subcutaneous tissue of rats and *S. sanguinis* were introduced. On day 3 post-introduction of *S. sanguinis*, the infectious sites were irradiated with NIR (808 nm, 0.5 W/cm^2). After post-operation for 7 days, the rats were sacrificed (Fig. 7A). As depicted in Fig. 7B, an infectious wound was still present in the control group. And the wound area in the Ti-SnS_2/I group was reduced compared to the Ti-U@SnS_2 group, while the Ti-U@SnS_2/I group had the best therapy efficiency. Then, the Giemsa staining was carried out to evaluate the bacteria infection (Figs. 7C and D). Large amounts of bacteria remained in the tissues in the control group and Ti-U@SnS_2 group. That might be since Ti-U@SnS_2 were no antibacterial action. While the amounts of bacteria residues were significantly lower in the Ti-SnS_2/I group and Ti-U@SnS_2/I group than

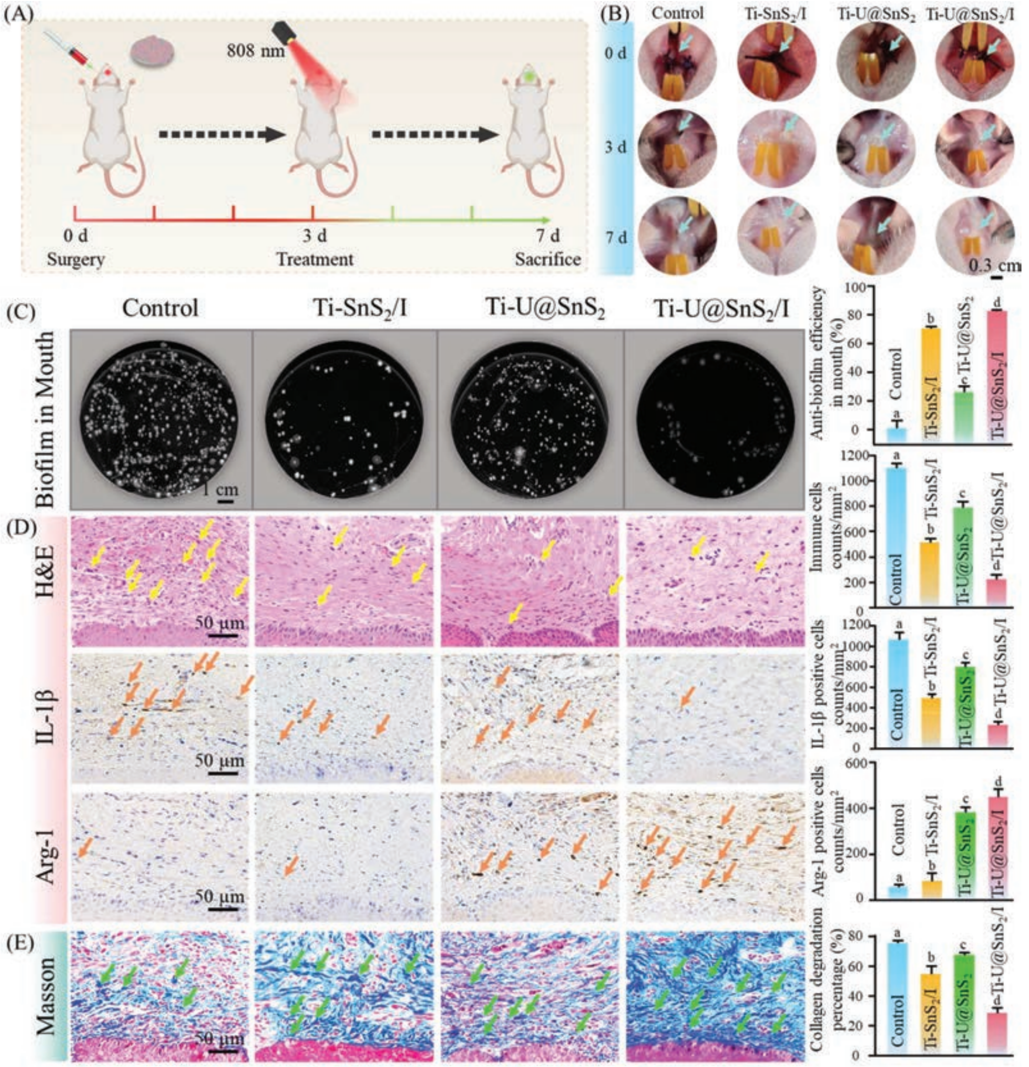

Fig. 6. Efficacy of Ti-U@SnS$_2$/I in the treatment of peri–implantitis in animal models. (A) Schematic diagram of modeling, administration, and final evaluation of peri–implantitis in rats. (B) Intraoral photographs of peri–implantitis rats with different surface-modified Ti sheets at the 3rd and 7th day. (C) Colony-forming images and the relative quantification data of surrounding tissue after 7 days. (D) H&E stain, IHC stains, and their relative quantification data of surrounding tissue after 7 days. The yellow arrows in (D) indicate immune cells. Orange arrows in (D) by staining brown indicate the inflammatory-related factors. Different letters represent statistical differences between each other. (E) Masson stains and the relative quantification data of surrounding tissue after 7 days, and green arrows in (E) indicate the related collagenous fibers ($n = 3$, $P < 0.05$).

control groups, especially in the Ti-U@SnS$_2$/I group. That might be attributed to ROS generation. Furthermore, the O_2 production of Ti-U@SnS$_2$/I enhanced its aPDT treatment. The Ti-U@SnS$_2$/I group also had the fewest bacterial colonies with an antibacterial efficiency of 84.7% (Fig. S10 in Supporting information). This finding was consistent with the trend in the results of intra-oral CFU quantification. In addition, the tissues around the Ti sheets were observed by H&E Masson staining. As shown in Figs. 7E-H, the control group had a significant immune inflammatory infiltration and irregular collagen fibrils, whereas the tissues of the Ti-U@SnS$_2$/I and Ti-SnS$_2$/I groups had less inflammatory cell infiltration. Particularly, the Ti-U@SnS$_2$/I group had the minimum number of inflammatory cells. The Ti-U@SnS$_2$/I group also displayed obvious fibrous tissue proliferation with uniform. That demonstrated that Ti-U@SnS$_2$/I possessed excellent biofilm ablation and immunoregulation. And interestingly, the titanium plates were embedded under the dermis of the rats' back skin in this experiment and were more than 5 mm deep here. This depth was much higher than the depth of the root tip of the implant. But the NIR still penetrated the skin to the depth of the infection and activated the nanoparticles with high efficiency. This indicated that the nanoparticles could tackle deeper infections of peri–implantitis.

In summary, we presented a smart and multi-functionalized implant nano-coating by co-encapsulating UCNPs, SnS$_2$, and ICG on the titanium surface for enhanced aPDT/CO-releasing synergistic treatment against peri–implantitis. The nano-coating could release O_2 and CO under NIR irradiation. The enhanced aPDT *via* O_2 generation could effectively eliminate biofilm and kill bacteria. Then the released CO could block the NF-κB pathway by controlling the production of the NF-κB inhibitor protein (IκBα), and it could regulate macrophage M1 and M2 polarization, impacting the inflammatory immune response. *In vivo*, the Ti-U@SnS$_2$/I implant nano-coating also exhibited remarkable synergistic antibacterial and anti-inflammatory capacity. Importantly, the Ti-U@SnS$_2$/I NSs with excellent synergic anti-microbial and anti-inflammatory properties also possessed great biocompatibility. In conclusion, as an effective strategy, Ti-U@SnS$_2$/I NSs have provided beneficial strategies for *in situ* bacterial killing and microenvironment regulation, which shows great application prospects in the field of peri–implantitis therapy. In addition, to offering a promising strat-

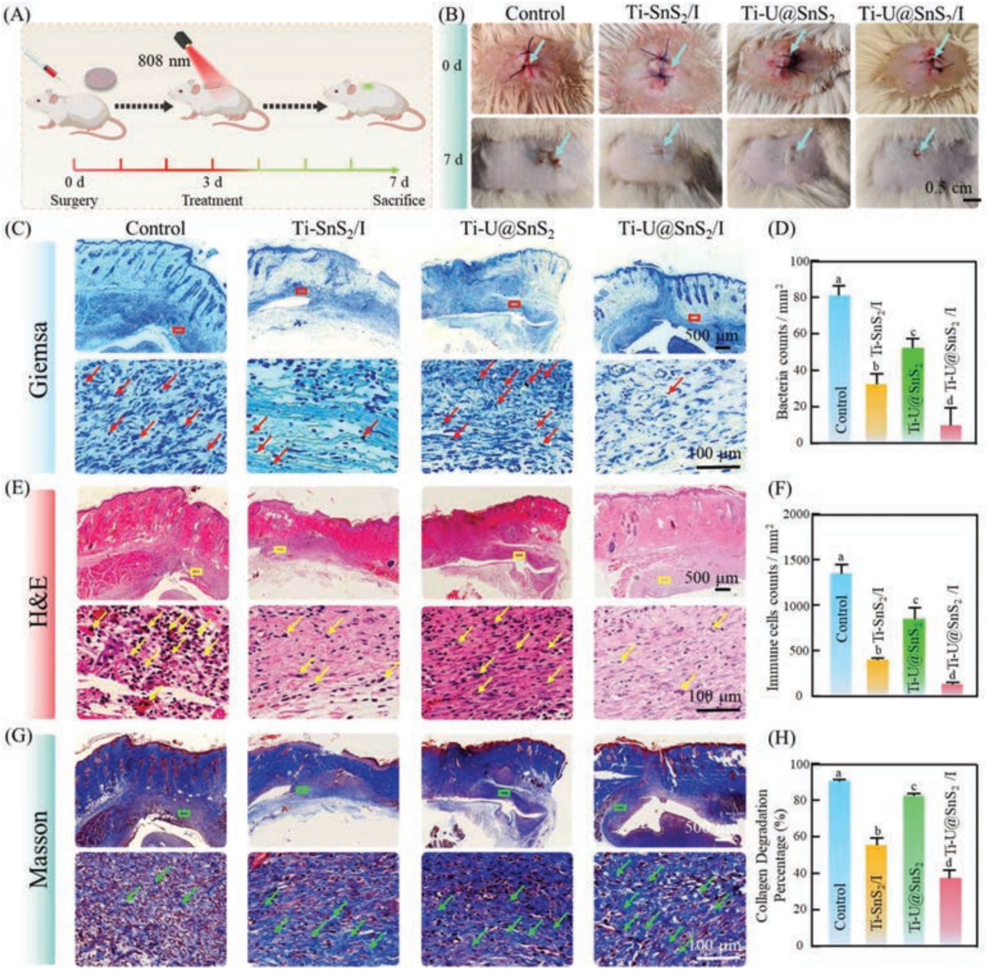

Fig. 7. Efficacy of Ti-U@SnS$_2$/I in the treatment of back implant infection in animal models. (A) Schematic diagram of modeling, administration, and final evaluation of back implant infection in rats. (B) Images of different surface-modified Ti sheets implanted subcutaneously on the infected back of rats on day 1 and day 7. Giemsa stain (C), H&E stain (D) Masson stain (E) of peri–tissue after six days. (D) The collagen volume in Masson staining, (F) corresponding immune cell counts per square millimeter in Histological evaluation, and (H) the relative number of bacteria in Giemsa staining sections. Red boxes and arrows in (C) indicate the related bacteria particles, yellow boxes arrows in (E) indicate the related immune cells, and green boxes and arrows in (G) indicate the related collagenous fibers. Different letters represent statistical differences among each group ($n = 3$, $P < 0.05$).

egy for the clinical prevention and treatment of peri–implantitis, Ti-U@SnS$_2$/I nano-coating is expected to play an irreplaceable implication for other medical implants for frequent and severe infectious complications, such as prosthetics, catheters, and several other devices.

Declaration of competing interest

The authors declare that they have no known competing financial interests or personal relationships that could have appeared to influence the work reported in this paper.

Acknowledgments

The authors acknowledge the National Natural Science Foundation of China (Nos. 82170998, 82201102, 62205122), the Postdoctoral Science Foundation Project of China (No. 2022M721316), the General program of the Natural Science Foundation of Jilin Province (Nos. YDZJ202201ZYTS017, 20220203145SF, 20210203087SF, YDZJ202201ZYTS274, YDZJ202201ZYTS080), Hygiene and Health Appropriate Technology Promotion Project of Jilin Province (No. 2020S014), the Science and Technology Project of Jilin Province Financial Department (Nos. jcsz2021893-21, jcsz2021893-15, ZkjcD105181350043103358), Science and Technology Project of Jilin Province Education Department (No. JJKH20221098KJ), and the Health Department Research Projects of Jilin Province (No. 2022JC076) for financial support.

Supplementary materials

Supplementary material associated with this article can be found, in the online version, at doi:10.1016/j.cclet.2023.108648.

References

[1] P.A. Norowski Jr, J.D. Bumgardner, J. Biomed. Mater. Res. B 88B (2009) 530–543.
[2] G.A. Kotsakis, D.G. Olmedo, Periodontol 86 (2021) 231–240.
[3] X. Li, M. Qi, X. Sun, et al., Acta Biomater. 94 (2019) 627–643.
[4] X. Li, M. Qi, C. Li, H.H.K. Xu, et al., J. Mater. Chem. B 7 (2019) 6955–6971.
[5] J. Fang, Y. Wan, Y. Sun, et al., Chem. Eng. J. 435 (2022) 134935.
[6] H. Moradpoor, M. Safaei, H.R. Mozaffari, et al., RSC Adv. 11 (2021) 21189–21206.
[7] M. Qi, X. Ren, W. Li, et al., Nano Today 43 (2022) 101447.
[8] Y. Sun, W. Xu, C. Jiang, et al., Front. Bioeng. Biotechnol. 10 (2022) 1074083.
[9] Z. Su, L. Kong, J. Mei, et al., Drug Resist. Update 67 (2023) 100917.
[10] M. Yang, H. Gong, D. Yang, et al., Chin. Chem. Lett. 34 (2023) 108468.
[11] S. Cheng, M. Pan, D. Hu, et al., Chin. Chem. Lett. 34 (2023) 108276.
[12] K. Chathoth, B. Martin, P. Cornelis, et al., FEMS Microbiol. Lett. 367 (2020) fnaa100.
[13] F. Li, Q. Pan, Y. Ling, et al., Chem. Eng. J. 460 (2023) 141791.
[14] D.L. Sai, J. Lee, D.L. Nguyen, et al., Exp. Mol. Med. 53 (2021) 495–504.
[15] J. Nart, R. Pons, C. Valles, et al., Clin. Oral Invest. 24 (2020) 675–682.
[16] X. Sun, J. Sun, Y. Sun, et al., Adv. Funct. Mater. 31 (2021) 2101040.

[17] A. Fakhri, S. Behrouz, M. Pourmand, J. Photoch. Photobio. B 149 (2015) 45–50.
[18] W. He, X. Wu, Y. Li, et al., Chin. Chem. Lett. 31 (2020) 2774–2778.
[19] K. Nakahira, A.M.K. Choi, Am. J. Physiol. Lung C 309 (2015) L1387–L1393.
[20] M. Wang, C.C. Mi, J.L. Liu, et al., J. Alloy. Compd. 485 (2009) L24–L27.
[21] L. Tong, X. Li, J. Zhang, et al., Sensor Actuat. B 246 (2017) 175–180.
[22] Y. Jiang, Z. Tan, T. Zhao, et al., Nanoscale 15 (2023) 1925–1936.
[23] X. Liu, M. Liu, J. Chen, et al., Chin. Chem. Lett. 29 (2018) 1321–1332.
[24] Z. Yang, Z. Min, B. Yu, Int. Rev. Immunol. 39 (2020) 292–298.
[25] H.P. Simmen, J. Blaser, Am. J. Surgery 166 (1993) 24–27.
[26] M.A. Lopez, P.C. Passarelli, M. Marra, et al., J. Biol. Regul. Homeost. Agents 34 (2020) 59–65.
[27] J. Derks, C. Tomasi, J. Oral Maxillofac. Res. 42 (2015) S158–S171.
[28] Y. Dai, Y. Ding, L. Li, Chin. Chem. Lett. 32 (2021) 2715–2728.
[29] S.T. Becker, B.E. Beck-Broichsitter, C. Graetz, et al., Clin. Implant Dent. R. 16 (2014) 401–411.
[30] Y. Wan, J. Fang, Y. Wang, et al., Adv. Healthc. Mater. 10 (2021) 2101515.
[31] C. Nathan, A. Cunningham-Bussel, Nat. Rev. Immunol. 13 (2013) 349–361.
[32] B. Zhou, X. Sun, B. Dong, et al., Theranostics 12 (2022) 2580–2597.
[33] Y. Li, Z. Xie, Y. Wang, et al., Can. J. Physiol. Pharm. 96 (2018) 922–928.
[34] B. Li, Y. Hu, Y. Zhao, et al., Front. Immunol. 8 (2017) 55.
[35] H.S. Kim, P.A. Loughran, J. Rao, et al., Am. J. Physiol. Gastr. L. 295 (2008) G146–G152.
[36] Y. Huang, T. Ma, Z. Ye, et al., Exp. Eye Res. 166 (2018) 29–39.
[37] M. Chhikara, S. Wang, S.J. Kern, et al., PLoS One 4 (2009) e8139.
[38] M. Paciolla, R. Boni, F. Fusco, et al., Hum. Reprod. 26 (2011) 1191–1201.
[39] T. Abduljabbar, Z. Akram, F. Vohra, et al., Clin. Implant Dent. Relat. Res. 20 (2018) 144–150.